https://doi.org/10.1016/j.ijthermalsci.2022.107795

Copper-alumina hybrid nanofluid droplet phase change dynamics over heated plain copper and porous residue surfaces

F.R. Siddiqui[1], C.Y. Tso[2], H.H. Qiu[1], Christopher Y. H. Chao[3,4], S.C. Fu[3*]

[1]Department of Mechanical and Aerospace Engineering, The Hong Kong University of Science and Technology, Hong Kong

[2]School of Energy and Environment, City University of Hong Kong, Hong Kong

[3]Department of Building Environment and Energy Engineering, The Hong Kong Polytechnic University, Hong Kong

[4]Department of Mechanical Engineering, The Hong Kong Polytechnic University, Hong Kong

*Corresponding Author Tel.: +852 2766 4858

E-mail Address: schung.fu@polyu.edu.hk

Postal Address: Department of Building Environment and Energy Engineering, The Hong Kong Polytechnic University, Hong Kong

Abstract

Droplet phase change is the key phenomenon for high heat transfer rates in spray or drop-wise cooling applications. Despite high cooling efficiency of the spray cooling technology, conventional fluids, such as water, cannot be used for thermal management of modern high heat flux devices due to their immense power density, resulting in early device failures. To address this issue, in this research, we experimentally study the evaporation performance for various volumes of the copper-alumina hybrid nanofluid (CAHF) droplet on a plain copper substrate and compare it with water (H_2O) droplet in sub-boiling and boiling regimes (i.e., for substrate temperatures of 25-170 °C). We also numerically investigate and compare the internal velocity and thermal fields of CAHF and H_2O droplets on a heated plain copper substrate. Besides the plain copper surface, we examine the phase change behaviour of the subsequent CAHF droplet over a heated residue surface that was obtained from the phase transition of the first CAHF droplet on a heated plain copper substrate. Our results demonstrate that the evaporation rate of CAHF droplets on a plain copper surface is up to 24% and an order of magnitude higher than water droplets in sub-boiling

and nucleate boiling regimes, respectively. Moreover, the evaporation rate of the CAHF droplet on a residue surface increases up to 141% and 800% compared to that on a plain copper surface in sub-boiling and nucleate boiling regimes, respectively. Furthermore, the latent heat flux up to 10 times can be achieved using the CAHF droplet compared to H_2O droplet on a plain copper substrate in the nucleate boiling region, making the CAHF a potential fluid for high heat flux cooling applications.

Keywords: Hybrid nanofluid, droplet phase change, heated residue, latent heat flux, Marangoni convection.

1. Introduction

Cooling technologies based on droplet evaporation, for instance spray cooling, offer much higher heat rejection rates than single-phase heat transfer processes. However, in recent years, heat generation in high heat flux devices has reached unprecedented levels (>100 W/cm^2) that cannot be thermally managed by existing thermal fluids due to their lower heat rejection capacity. This not only resulted in early device failures, but also inhibited the future growth of high heat dissipating devices, prompting a need to investigate advanced heat transfer fluids with high heat rejection capability. Such advanced fluids when used in efficient cooling technologies, for example spray cooling, may resolve thermal management issues in high heat flux applications. Conventional fluids, for instance water, can be transformed into highly efficient heat transfer fluids by adding a small fraction of nanometer-sized particles, known as nanofluids.

Nanofluids show a higher thermal conductivity than their respective base fluids due to the dispersed nanoparticles [1–5]. The nanofluid thermal characteristics depends on several factors, such as temperature, dispersion stability, base fluid and nanoparticle type, size, shape and concentration [6–8]. Although nanofluids possess advanced thermal characteristics due to high thermal conductivity, they do not exhibit all the necessary (rheological and thermal) properties needed in heat transfer applications [9]. For example, metal-oxide nanofluids exhibit higher dispersion stability but lower thermal conductivity than metal nanofluids. Conversely, metal nanofluids possess high thermal conductivity and exhibit poor dispersion stability. As nanofluids

do not possess all essential characteristics needed in heat transfer fluids, they cannot be used in their current form for effective cooling of high heat flux devices [10].

More recently, an advanced form of nanofluid was investigated with much better dispersion stability and thermal conductivity than single particle nanofluid and was named hybrid nanofluid [11–13]. Hybrid nanofluid is prepared by dispersing any two types of nanoparticles (from metal, non-metal or metal-oxide) in the base fluid. The advanced hydrodynamic and thermal properties of hybrid nanofluids mainly depend on their inter-particle compatibility [14]. The thermo-rheological characteristics of hybrid nanofluids comprising non-compatible nanoparticles are even worse than for single particle nanofluids. Moreover, the synergy between two compatible nanoparticle types leads to much higher thermal conductivity in hybrid nanofluids than single particle nanofluids [15–17]. The advanced thermo-rheological properties as well as inter-particle synergy in hybrid nanofluids are some of the desirable characteristics needed for high heat flux device cooling.

The hybrid nanofluid, as an emerging heat transfer fluid, has not yet received sufficient attention regarding its application in droplet evaporation or boiling based cooling processes. With inter-particle synergy and advanced thermo-rheological properties, hybrid nanofluid droplets may exhibit better heat removal rates compared to base fluid or single particle nanofluid droplets. Although droplet phase change on un-heated substrates has been widely studied for single particle nanofluids with a very limited focus on hybrid nanofluids [18–23], the hybrid nanofluid droplet phase change on heated surfaces received no attention to date by the research community. However, some researchers have studied the evaporation behaviour of single particle nanofluid droplets on heated surfaces. Research indicates higher evaporation rates for single particle nanofluid droplets compared to water droplets on heated substrates [24,25]. Al-Sharafi et al. [26] concluded that Marangoni forces dominate buoyancy forces in the CNT based nanofluid droplet on a heated substrate. In another study [27], they suggested that both Marangoni and buoyancy forces contribute to circulating vortices inside the CNT nanofluid droplet during its evaporation on a heated substrate.

Like evaporation, the hybrid nanofluid droplet boiling over heated surfaces was not previously investigated. However, some researchers have studied the boiling behaviour of single particle nanofluid droplets. Okawa et al. [28] reported significant enhancements in critical heat flux of TiO_2 nanofluid droplets compared to water droplets. Duursma et al. [29] reported 10% increase in heat flux of aluminium-dimethyl sulfoxide (DMSO) nanofluid droplet at 0.1% volume fraction compared to the pure DMSO droplet. Paul et al. [30] showed that TiO_2 nanofluid droplets exhibit much reduced evaporation time compared to water droplets at a surface temperature of 300 °C. They concluded that nanofluid droplets with high particle concentration do not show the Leidenfrost effect, and that these droplets release small droplets due to thermal agitation, resulting in higher evaporation rates than water droplets. The literature indicates that single particle nanofluids show enhanced heat flux and better droplet evaporation rates than their respective base fluids, however, they are not suitable for practical applications, as they do not exhibit overall thermo-rheological characteristics. Therefore, the phase change behaviour of hybrid nanofluid droplets should be investigated due to their better thermo-rheological properties than single particle nanofluids.

We recently showed [9] that copper-alumina hybrid nanofluid (CAHF) possesses better thermo-rheological properties (high dispersion stability and enhanced thermal conductivity) than corresponding single particle nanofluids (i.e., copper and alumina nanofluids) and therefore, CAHF may be a suitable candidate for droplet based cooling applications. As water is one of the most commonly used heat transfer fluids in high heat flux cooling applications, the key objective of this paper is to investigate and compare the evaporation and boiling performances of CAHF and water droplets for various droplet volumes on a plain heated copper substrate. In this paper, as higher evaporation rate is achieved for CAHF droplets compared to water droplets on a plain heated copper substrate, we numerically investigated and compared the internal velocity and temperature fields of evaporating CAHF and H_2O droplets. Furthermore, as a novelty, we studied the hybrid nanoparticle dynamics inside the CAHF droplet and compared its velocity field with the flow field of surrounding fluid molecules in the CAHF droplet. We also demonstrated the effects of the thermal Marangoni convection on internal velocity and thermal fields of the CAHF droplet that eventually improves its evaporation rate compared to H_2O droplet. Moreover, we compared the boiling dynamics of CAHF and H_2O droplets in the nucleate boiling region using a

high speed imaging technique. We also determined the droplet latent heat flux to assess the heat removal capability of CAHF droplets in comparison to H_2O droplets for potential application of the CAHF in high heat flux device cooling. We lately investigated the evaporation and boiling behaviour for silver graphene hybrid nanofluid droplet with respect to mixing ratios [31], however, our main focus in current study is to investigate the main differences and mechanisms involved in higher evaporation rates of CAHF droplets compared to H_2O droplets.

As the CAHF droplet phase change results in a porous residue formation over a heated copper surface, the effect of the heated residue surface on phase change behaviour of the subsequent CAHF droplet was also investigated. The residue effect is important to consider in hybrid nanofluid spray or drop-wise cooling applications, where residues from hybrid nanofluid droplet phase change over a heated substrate may affect the evaporation performance of subsequent incoming hybrid nanofluid droplets residing over such heated residue surfaces. Droplet residues were extensively studied in the past for different forms and patterns [32–35], however, the effect of heated residues on evaporation rate of following droplets has not been previously investigated. Although we recently investigated the residue effect on wetting and evaporation behaviour of following incoming hybrid nanofluid droplets [22,36], these studies were based on un-heated residue surfaces, where the hybrid nanofluid droplet evaporation was studied at room temperature. However, in the current research, we investigate the heated residue effect on phase change behaviour of the subsequent CAHF droplet. The main objectives of this research can be summarized as:

- To investigate and compare the evaporation and boiling performances of CAHF and water droplets for various droplet volumes on a heated copper substrate.
- To study and compare the internal velocity and temperature fields of CAHF and H_2O droplets for copper surface temperatures up to T_s = 100 °C.
- To examine the effect of a heated residue surface on phase change behaviour of the subsequent CAHF droplet in comparison to a plain heated copper surface.

2. Experimental test facility

The copper-alumina hybrid nanofluid (CAHF) was prepared by dispersing copper (particle size of 25 nm) and alumina nanoparticles (particle size of 13 nm) in the de-ionized water followed by ultrasonication using an ultrasonic bath (Model 2510, Branson, USA) for 0.5 hours [7]. As large sized nanoparticles can sediment faster than small nanoparticles resulting in reduced dispersion stability and low thermal conductivity, small sized copper and alumina nanoparticles were selected in current research. The CAHF was prepared for a fixed mixing ratio of 0.5(Cu):0.5(Al_2O_3), as it exhibits better hydro-thermal characteristics (improved dispersion stability and high thermal conductivity) than other mixing ratios, as reported in our recent research [9]. Moreover, as hybrid nanofluids show enhanced thermal properties at very low particle concentration, the CAHF was synthesized at a low volume fraction of 0.1%. To investigate CAHF thermal conductivity enhancement in comparison to de-ionized water, the thermal conductivity of CAHF and H_2O samples was measured at different temperatures using a thermal conductivity analyser setup (TPS 500S, Hot Disk, Sweden). The detailed experimental setup for CAHF thermal conductivity measurements is demonstrated in our recent study [9]. The surface tension (used in numerical modelling and to determine Marangoni and dynamic Bond numbers) at various temperatures was subsequently measured by using 5 µl volume of H_2O and CAHF pendant droplets at 1.4 frames per second and time duration of 20 seconds in a contact angle meter (Theta, Biolin Scientific, Finland). Each measurement was performed three times to reduce uncertainties in results. Later, the surface tension gradient was obtained by processing measured surface tension data against different temperatures. The surface tension gradient was implemented as an input parameter to incorporate the effect of thermal Marangoni convection in our model.

Following the thermal conductivity and surface tension measurements, the droplet phase change experiments were conducted in an environmental test chamber, where the relative humidity (RH) and ambient temperature (T_a) were fixed at $RH = 0.3 \pm 0.03$ and $T_a = 25 \pm 0.3$ °C, respectively. The schematic of the experimental setup used to study the evaporation of CAHF and H_2O droplets on a heated copper substrate is illustrated in Fig. 1 (a). A 0.1 m x 0.15 m silicone heater mat (RS, UK) with a power of 100 W was used to heat the base of a 0.05 m x 0.06 m copper plate, while the copper plate surface temperature was measured using two T-type thermocouples (RS, UK). Each thermocouple was placed near the opposite ends of a copper surface. A Teflon strip, screwed

at both ends, was used to fix each thermocouple on a copper surface such that the thermocouple was sandwiched between the Teflon strip and a copper surface, as illustrated in Fig. 1 (a). The air gap between the Teflon strip and the copper surface was filled with silicone thermal grease (RS, UK). To ensure better thermal contact, the thermal grease was also applied between the heater and the copper base. The temperature of the copper surface was increased from room temperature (25 °C) up to 170 °C by connecting the heater to an adjustable AC power supply. The droplet evaporation process was recorded at 30 frames per second (fps) using a video camera. In the nucleate boiling region, the boiling dynamics of CAHF and H_2O droplets was investigated using a high speed camera (HG-100K, Redlake, USA) at frame rates ranging between 60 fps and 500 fps. Moreover, the droplet surface temperature during the evaporation process was measured using an infrared camera (Ti25, Fluke, US). The infrared camera was calibrated using a T-type thermocouple by measuring the surface temperature of water and CAHF samples in a 10 ml glass beaker at every 5 °C increment in a temperature range of 30-50 °C. The maximum error between the thermocouple and IR camera was 1.3 °C and 1.8 °C for the CAHF and water samples, respectively, at an emissivity of 0.98. This error increased at other values of emissivity.

A micropipette was used to carefully dispense the first CAHF droplet of known droplet volumes of V_{fd} = 3, 15, 30 and 60 µl over a plain copper substrate at a pre-set surface temperature. The droplet evaporation time was determined from a video camera recording for entire droplet phase change process. The droplet evaporation rate was obtained by dividing the known initial droplet volume by net droplet evaporation time. As the first CAHF droplet evaporated (V_{fd} = 3, 15, 30 and 60 µl), a residue surface was formed corresponding to each droplet volume from the first CAHF droplet of V_{fd} = 3, 15, 30 and 60 µl. Subsequently, second CAHF droplet of fixed droplet volume as V_{sd} = 3 µl was dispensed over each residue surface obtained from first droplet volumes of V_{fd} = 3, 15, 30 and 60 µl. As a result, four different droplet volume ratios were obtained as V_{fd}/V_{sd} = 3µl/3µl=1, 15µl/3µl=5, 30µl/3µl=10 and 60µl/3µl=20.

These experiments were conducted three times to reduce measurement uncertainties. Moreover, as the evaporation rate of a 3 µl CAHF droplet on its residue surface for the droplet volume ratio of V_{fd}/V_{sd} = 1 was similar to that obtained on a plain copper surface, the results are only presented for droplet volume ratios of V_{fd}/V_{sd} = 5, 10 and 20 in results and discussion section (Section 4).

Furthermore, as the same copper surface is used for both CAHF and H_2O droplets, the copper surface characteristics may equally affect the evaporation rates for CAHF and H_2O droplets.

3. CAHF droplet simulation

The internal velocity and thermal field distribution for heated CAHF and H_2O droplets were investigated by developing a numerical model using COMSOL Multiphysics. As the suspended copper-alumina hybrid nanoparticles are difficult to visualize even using experimental techniques, such as particle image velocimetry (PIV), we developed a numerical model to investigate the hybrid nanoparticle trajectory and compare the internal velocity and temperature fields between CAHF and H_2O droplets. The droplet model was built using a non-isothermal flow interface that couples the flow and heat transfer interfaces within the droplet. Due to the symmetry of considered sessile droplets along the vertical axis, a two dimensional axisymmetric geometry was developed from an original droplet image at different time instants during the droplet evaporation using ImageJ software. Furthermore, a laminar flow condition was used inside the droplet domain due to extremely low Rayleigh number ($< 10^{-3}$) for studied substrate temperatures of 60-100 °C.

The CAHF thermophysical properties were defined using well-developed theoretical models for hybrid nanofluids [9,11]. As the main objective of our model was to investigate the internal flow and temperature fields at instantaneous steady-state points during droplet evaporation, the transient evaporation effects were neglected at the droplet-air interface. Due to the high surface tension gradient for CAHF and H_2O droplets (as illustrated in Fig. 3 (a)), the thermal Marangoni effect along with buoyancy effect were also considered in our model. The surface tension gradient was used as an input parameter to solve thermal Marangoni convection in our model. The Marangoni effect was implemented in our model using the Marangoni Effect Mutiphysics coupling. This coupling considers the Marangoni induced flow along the droplet-air interface that results from the temperature difference between the droplet three phase contact line and droplet apex. On the other hand, the buoyancy effect was implemented in our model by considering the Boussinesq approximation in the Navier-Stokes equation. The Boussinesq approximation accounts for buoyancy induced flow that results due to the fluid density difference between the droplet-solid interface (due to the heated surface) and droplet apex. Moreover, in our model, the Navier-Stokes equation was solved using the laminar flow interface given as:

$$\rho(V.\nabla V) = -\nabla p + \nabla.\left(\mu(\nabla V + (\nabla V)^T) - \frac{2}{3}\mu(\nabla.V)\right) + \rho g \quad (1)$$

where p is the pressure and μ is the dynamic viscosity of the SGHF. Moreover, the energy equation in our model was solved using the heat transfer in fluids interface, as given by following equation:

$$\rho C_p V.\nabla T = \nabla.(k\nabla T) + Q + Q_p + Q_{vd} \quad (2)$$

where C_p is the specific heat capacity, k is the thermal conductivity of the considered SGHF, $Q_p = -\frac{1}{\rho}\frac{\partial \rho}{\partial T}T\left(\frac{\partial p}{\partial T} + V.\nabla p\right)$ is the pressure term and $Q_{vd} = \tau:\nabla V$ is the viscous dissipation term. Q is the user-defined energy generation term that involves additional heat sources other than pressure and viscous dissipation terms. The viscosity of hybrid nanofluids depends on nanoparticle concentration and can be estimated as [37]:

$$\mu_{hnf} = (1 + 2.5\phi + 6.2\phi^2)\mu_{bf} \quad (3)$$

Where ϕ is the volume fraction of hybrid nanoparticles and μ_{bf} is the dynamic viscosity of base fluid (water). We used equation (3) to set viscosity of hybrid nanofluids as an input parameter in our model. As increased concentration (or volume fraction,ϕ) of hybrid nanoparticles during CAHF droplet evaporation increases its viscosity, the viscosity variation for different time instants of CAHF droplet evaporation was considered in our model. Moreover, the variation in hybrid nanoparticle concentration (ϕ) was determined from the variation in droplet volume (using IR imaging data) during evaporation that was used in equation (3) to determine the CAHF droplet viscosity.

The dynamics of suspended hybrid nanoparticles inside the CAHF droplet was simulated using the particle-tracing module. The drag (F_d), lift (F_l), gravity (F_g) and thermophoretic (F_{tf}) forces that affect the hybrid nanoparticle trajectory were all included in our model. These forces were determined as [38–40]:

$$F_d = -6\pi\mu_{bf} r\Delta V \quad (4)$$

$$F_l = K\mu_{bf} r^2 \Delta V \sqrt{\frac{\dot{\gamma}}{v}} \quad (5)$$

$$F_g = m_{np} g \left(\frac{\rho_{np} - \rho_{bf}}{\rho_{np}}\right) \quad (6)$$

$$F_{tf} = -\frac{12\pi r C_s \nabla T (k_{np}/k_{bf}) {\mu_{bf}}^2}{T[2(k_{np}/k_{bf})+1]\rho_{bf}} \quad (7)$$

where r is the nanoparticle radius, ΔV is the relative velocity between the fluid and the nanoparticle, K is a constant and is equal to 81.2, $\dot{\gamma}$ is the shear rate, v is the kinematic viscosity, m_{np} is the mass of nanoparticle, g is the acceleration due to gravity, ρ_{np} and ρ_{bf} are densities of nanoparticle and base fluid, respectively, C_s is a constant equal to 1.17, T is temperature, and k_{np} and k_{bf} are thermal conductivities for nanoparticle and base fluid, respectively. These forces were not incorporated in the Navier-Stokes equation, as hybrid nanofluid was treated as a continuum fluid in equation (1). However, these forces were considered in the particle-tracing module of COMSOL Multiphysics, where hybrid nanoparticle trajectories were investigated inside the CAHF droplet. Moreover, the Brownian force was neglected in our study, as it had a negligible effect on studied hybrid nanoparticle velocity field. This is because thermophoretic forces may have a more dominant effect on studied hybrid nanoparticle dynamics due to temperature gradient effects inside the CAHF droplet compared to Brownian forces. Some other researchers also reported the significant effect of thermophoresis up to two orders of magnitude compared to the Brownian diffusion in heated systems [40,41]. Moreover, the Brownian force significantly increased the computational time of our numerical modelling.

The free triangular mesh was used due to simple two-dimensional axisymmetric geometry of considered droplets. In order to develop a computationally inexpensive model, the mesh independence study was conducted for a droplet volume of 3µl, as shown in Fig. 1 (b). It is noticed that increasing the mesh elements from 881 to 6139 considerably affects the internal velocity magnitude along the normalized droplet height. However, further increasing the mesh elements does not considerably affect the velocity profile. Therefore, we used 6139 mesh elements

303 comprising extra-fine mesh at droplet boundaries and finer mesh in other areas of the droplet
304 domain.
305
306 ***3.1. Boundary Conditions***
307 The realistic boundary conditions were considered in the model by using our experimental data at
308 different time instants during the droplet evaporation process. The temperature at the droplet-solid
309 interface boundary was obtained from the measured copper surface temperature, while the
310 temperature at the droplet-air interface boundary was obtained using the infrared imaging
311 temperature data (as discussed in the supplementary material). In this way, the variation in droplet
312 shape as well as boundary conditions at the droplet-air interface boundary for different time
313 instants during the droplet evaporation process were reproduced in our model. Furthermore, the
314 slip and no-slip boundary conditions were used at droplet-air and droplet-solid interfaces,
315 respectively. Although no-slip boundary condition at droplet-solid interface does not much affect
316 the internal convection in a heated CAHF droplet (as illustrated in Fig. 2 (a) and Fig. 2 (b)), it was
317 still considered in our model since the flow velocity at droplet-solid interface must be equal to
318 zero. At droplet-air interface, the slip boundary condition was considered by setting a no
319 penetration condition ($\mathbf{V}.\mathbf{n} = 0$) and non-viscous effects resulting in no boundary layer at droplet-
320 air interface.
321
322 ***3.2. Model Validation***
323 We validated our water droplet numerical model using the particle image velocimetry (PIV) data
324 for heated water droplets presented by Karlsson et al. [42], as demonstrated in Fig. 1 (c). From
325 contact radius and droplet height data [42], the two dimensional droplet model was developed
326 using spherical cap equations. The spherical cap assumption was used for a reason that the contact
327 radius did not exceed the capillary length for the water droplet examined by Karlsson et al. [42].
328 During the model validation, both Marangoni and buoyancy effects were considered. The no-slip
329 and slip boundary conditions were used at droplet base and the droplet-air interface, respectively.
330 In Fig. 1 (c), it is noticeable that our model satisfactorily estimates the velocity profile along the
331 droplet height for droplet evaporation time of t = 1-15 s at surface temperatures of 313.15 K and
332 323. 15 K. However, small differences between the estimated and PIV results may be due to the

simplified assumptions in our model, such as neglecting convection currents around the droplet-air interface or ignoring mass diffusion from droplet surface into the air.

4. Results and discussion

4.1. Evaporation performance of CAHF droplets compared to H_2O droplets

The evaporation rate for different substrate temperatures and droplet volumes of CAHF and H_2O droplets is shown in Fig. 2 (c). A significant increase in droplet evaporation rate can be observed with increasing droplet volume and copper surface temperature. The CAHF droplet evaporation rate increases up to 235% on a heated copper surface with increasing droplet volume in a range between 3 µl and 60 µl. This is for a reason that the droplet-solid and droplet-air interfacial areas increase with increasing droplet volume. Large droplet contact area results in high heat transfer rates between the droplet and the substrate, while large droplet-air interface area increases the mass transfer from droplet surface into the surrounding air. Due to this reason, the net evaporation rate tremendously increases with increasing droplet volume. Furthermore, the CAHF droplet evaporation rate increases up to 24% compared to H_2O droplet on a heated copper surface for temperatures between 25 °C and 100 °C, as shown in Fig. 2 (c). The higher evaporation rate for the CAHF droplet over a heated copper surface is possibly due to its higher thermal conductivity than H_2O droplet (discussed in Section 4.1.1). Moreover, the suspended hybrid nanoparticles in the CAHF droplet may also modify the internal flow and temperature fields (discussed in Section 4.1.1), thus resulting in higher evaporation rates than H_2O droplets. The evaporation rate for both CAHF and H_2O droplets on copper substrate can be estimated from the following empirical equation:

$$E = aE_o\left(\frac{T_s}{T_b}\right)^b \tag{8}$$

where T_b is the droplet temperature at its boiling point (T_s = 100 °C), E_o is the evaporation rate of smallest considered droplet volume (V_o = 3 µl) over a copper substrate at room temperature of 25 °C, the coefficient $a = C_1(V/V_o)^{C_2}$ and constant b = 3. V is any droplet volume in a range of 3-60 µl, constants C_1 and C_2 are equal to 67.318 and 0.386 for CAHF droplets while these are equal to 65.907 and 0.377 for H_2O droplets, respectively. The values of these constants may depend on

363 fluid thermal properties and are obtained from the experimental data of Fig. 2 (c). It was also
364 observed in our experiments that both CAHF and H_2O droplets were pinned throughout
365 evaporation thus exhibiting constant contact diameter (CCD) mode of evaporation. For CAHF
366 droplets, this may be due to the hybrid nanoparticle migration towards the droplet three-phase
367 contact line (driven by internal convection currents) that pinned the CAHF droplet resulting in
368 CCD mode of evaporation. This also suggests that hybrid nanoparticles driven by internal
369 convection currents deposit near the droplet three-phase contact line resulting in a pinning effect
370 for CAHF droplet. For water droplets, the CCD mode of evaporation is possibly due to the natural
371 convection and Marangoni forces that might have pinned the droplet on a heated surface.
372 Moreover, the evaporation rate for CAHF droplets obtained in this study is almost similar to that
373 reported by Xu et al. [43] for gold nanofluid droplets at similar droplet volumes and substrate
374 temperatures. This is because hybrid nanofluid droplets do not exhibit significantly high
375 evaporation rates at low substrate temperatures (i.e., $T_s < 60$ °C) possibly due to reduced internal
376 convection effects. In another study by Yan et al. [44], the top heating of gold nanofluid droplets
377 using solar energy resulted in similar evaporation rates as that obtained for CAHF droplets in
378 current study. However, they showed that side heating of gold nanofluid droplets reduced
379 evaporation rates up to 20% than that obtained in current study for similar droplet volumes and
380 droplet surface temperatures, respectively. Furthermore, the evaporation rate of CAHF droplet at
381 substrate temperature of T_s = 105 °C is 13% higher than that reported by Kim [25] for CuO
382 nanofluid droplet for similar droplet volumes. However, they used nanoparticle concentration of
383 0.5% volume fraction in comparison to just 0.1% volume used in current study. Besides different
384 experimental conditions used in these studies, higher evaporation rates for hybrid nanofluid
385 droplets may be due to better heat transfer properties compared to mono nanofluids, as already
386 discussed in introduction section of this study. Furthermore, the main mechanisms involved for
387 improved evaporation rates of CAHF droplets are discussed in Section 4.1.1.

388

389 Fig. 2 (d) shows the evaporation rate of a 3 µl CAHF droplet resting over plain copper and porous
390 residue surfaces for various residue sizes and surface temperatures. It is noticeable that the
391 evaporation rate of the following CAHF droplet on its heated residue surface for V_{fd}/V_{sd} = 5
392 significantly increases up to 112% compared to a heated plain copper surface for surface
393 temperatures of T_s = 25 - 100 °C. Further increasing the droplet volume ratio above V_{fd}/V_{sd} = 5

increases the evaporation rate of the CAHF droplet up to 141% compared to a copper surface. This is for a reason that the CAHF droplet spreads on its partially wetting residue surface, exhibiting large droplet-solid and droplet-air interfacial areas, which subsequently results in its high droplet evaporation rate. On the other hand, the CAHF droplet resting on a non-wetted copper surface exhibits a low droplet contact area, resulting in relatively lower evaporation rates compared to the CAHF droplet residing over its partially wetted residue surface. The wettability effect of un-heated droplet residue on subsequent droplet evaporation rate is demonstrated in our previous study [36]. Furthermore, the enhanced evaporation rate of the CAHF droplet over a heated plain copper surface as compared to H_2O droplet (as illustrated in Fig. 2 (c)) is mainly attributed to suspended hybrid nanoparticles, which may modify the internal velocity and thermal field distribution of the CAHF droplet, as further discussed in Section 4.1.1.

4.1.1. Mechanistic behavior of improved evaporation performance for CAHF droplets

4.1.1.1. Thermal conductivity and surface tension effects

Fig. 3 (a) illustrates the CAHF thermal conductivity enhancement with respect to water (base fluid) at different temperatures. It can be noticed that the CAHF thermal conductivity considerably increases with increasing temperatures, exhibiting enhancement up to 15.5% at T = 70 °C. This is due to enhanced thermal properties of suspended copper-alumina hybrid nanoparticles that increase the overall CAHF thermal conductivity. The CAHF thermal conductivity enhancement can be estimated using the following non-dimensional empirical equation:

$$k_{en} = ae^{b\left(\frac{T}{T_o}\right)} \tag{9}$$

where T_o = 20 °C is the reference (minimum) temperature for measured thermal conductivity in this study while coefficients a = 0.0482 and b = 1.6218 are obtained from measured thermal conductivity data points (shown by red markers in Fig. 3 (a)).

4.1.1.2. Droplet internal convection effects

The convection effects inside the CAHF and H_2O droplets are investigated using the dynamic Bond number [$Bo_d = \rho g \beta h^2/(-d\gamma_{lv}/dT)$], where h is the droplet height, $d\gamma_{lv}/dT$ is the surface tension

gradient (obtained from Fig. 3 (a)), ρ and β are the density and volumetric thermal expansion coefficient, respectively, obtained as $\rho = 0.5\phi\rho_{Cu} + 0.5\phi\rho_{Al2O3} + (1-\phi)\rho_{H2O}$ and $\beta = -1/\rho(d\rho/dT)$ at $[T(y = 0)+T(y = h)]/2$. The dynamic Bond number shows the relative strength of buoyancy and Marangoni forces within a heated droplet. Fig. 3 illustrates the dynamic Bond number variation in CAHF and H_2O droplets with normalized droplet evaporation time (t/t_o), where t_o is the net droplet evaporation time. As $Bo_d < 1$ during the droplet evaporation, the Marangoni forces dominate buoyancy forces in both CAHF and H_2O droplets. Moreover, increasing droplet volume increases the dynamic Bond number suggesting a rise in buoyancy forces. However, as $Bo_d < 1$, the buoyancy forces are still not strong enough to overcome thermal Marangoni forces within the evaporating CAHF and H_2O droplets. It is also noticeable that the dynamic Bond number decreases during the course of droplet evaporation indicating further weakening of the buoyancy forces. Moreover, the dynamic Bond number is slightly higher for CAHF droplets than for H_2O droplets. This suggests that buoyancy forces are marginally stronger in CAHF droplets possibly due to higher density and volumetric expansion coefficient than that of H_2O droplets. These results also indicate that the thermal Marangoni forces may affect the internal velocity and thermal field distribution of CAHF and H_2O evaporating droplets. Therefore, both Marangoni and buoyancy effects were considered in our droplet numerical model.

Fig. 4 shows the variation of the Marangoni number with respect to normalized droplet evaporation time (t/t_o). The Marangoni number is determined as $Ma = h\Delta T(-d\gamma_{lv}/dT)/\mu\alpha$, where h is the droplet height, ΔT is the temperature difference between the droplet apex and three-phase contact line obtained using an infrared imaging (discussed in supplementary material), $d\gamma_{lv}/dT$ is the temperature dependent surface tension gradient obtained from Fig. 3 (a), α is the thermal diffusivity and μ is the dynamic viscosity (both α and μ were obtained at $[T(y = 0)+T(y = h)]/2$). It is observed in Fig. 4 that the Marangoni number decreases with increasing droplet evaporation time suggesting a reduction in thermal Marangoni convection for both CAHF and H_2O droplets, as illustrated in Fig. 4. Furthermore, the Marangoni number considerably increases with increasing droplet volume and substrate surface temperature. It is also noticeable that the Marangoni number in the CAHF droplet mostly remains higher than H_2O droplet during the droplet evaporation process. This suggests that enhanced thermal Marangoni convection, besides high thermal conductivity, contribute towards higher evaporation rate in CAHF droplets compared to H_2O

455 droplets on a plain heated copper surface, as demonstrated in Fig. 2 (c). However, it is pertinent to
456 also compare the internal velocity and temperature fields of CAHF and H_2O droplets, as
457 demonstrated in Fig. 5 and Fig. 6.
458
459 *4.1.1.3. Internal velocity and thermal field distribution of CAHF and H_2O droplets*
460 Fig. 5 (a) and (b) show the comparison of internal velocity and thermal field distribution between
461 the CAHF droplet (droplet left half) and H_2O droplet (droplet right half) on a plain heated copper
462 surface for T_s = 60 °C at the beginning of droplet evaporation process (t = 1s). Although both
463 CAHF and H_2O droplets exhibit similar vortices in Fig. 5 (a), high velocity magnitude (shown by
464 red colour) can be observed near the three-phase contact line of the CAHF droplet. This may be
465 due to higher Marangoni convection in the CAHF droplet as compared to H_2O droplet, as
466 demonstrated in Fig. 4. A well-mixed internal flow is developed due to high velocity magnitude
467 inside the CAHF droplet resulting in relatively lower average internal temperature (light yellow
468 colour in droplet left half of Fig. 5 (b)) than that of water droplet (dark yellow colour in droplet
469 right half of Fig. 5 (b)). Moreover, Fig. 5 (a) shows that the flow direction is the same (from the
470 droplet three-phase contact line towards the droplet apex) for both CAHF and H_2O droplets. This
471 flow direction also indicates that high Marangoni stresses (as discussed in Fig. 4) move the fluid
472 along the thermal gradient on droplet surface. i.e., from a low surface tension region (droplet three-
473 phase contact line) towards a high surface tension region (droplet apex). Moreover, the suspended
474 copper (pink particles) and alumina (blue particles) nanoparticles follow the same flow direction
475 as surrounding fluid molecules, as illustrated in droplet left half of Fig. 5 (a). Furthermore, the
476 alumina nanoparticles exhibit higher velocity than copper nanoparticles, as shown by long blue
477 particle tails compared to short pink particle tails in Fig. 5 (a) inset. This is because of the low
478 density and small diameter of an alumina nanoparticle compared to a copper nanoparticle.
479
480 Fig. 5 (c) and (d) show fluid internal velocity and thermal field for CAHF and H_2O droplets at time
481 t = 20 s of the droplet evaporation process, respectively. The higher velocity magnitude can be
482 observed for the CAHF droplet near the droplet-air interface and vertical axis of symmetry
483 compared to H_2O droplet. Although Marangoni forces decrease with increasing droplet
484 evaporation time (as illustrated in Fig. 4), these are still stronger in the CAHF droplet, resulting in
485 higher velocity magnitude compared to H_2O droplet. A well-mixed internal flow due to high

velocity magnitude in the CAHF droplet develops a low temperature region near the vertical axis of symmetry, as demonstrated by a light-yellow region in droplet left half of Fig. 5 (d). It is noticeable that hybrid nanoparticles move away from the high temperature zone near the droplet-solid interface (red region in Fig. 5 (d)) due to high wall shear stress and enhanced thermophoretic forces. This results in a concentration gradient with higher concentration of hybrid nanoparticles in the vortex region compared to droplet vertical axis of symmetry and interfacial (droplet-solid and droplet-air) regions, as illustrated in Fig. 5 (c). Conversely, hybrid nanoparticles are uniformly distributed inside the CAHF droplet at the beginning of its evaporation (t = 1s), as observed in Fig. 5 (a).

The fluid flow and temperature fields for CAHF and H_2O droplets at time t = 40 s of droplet evaporation is demonstrated in Fig. 5 (e) and (f). It can be observed that the peak velocity magnitude in the CAHF droplet decreases during its evaporation (low at t = 20 s and t = 40 s as compared to t = 1 s). This may be due to increased nanoparticle concentration that increases the viscosity of the CAHF droplet (as shown in equation (3)) during its evaporation. However, due to high thermal Marangoni stress, the velocity magnitude near the droplet three-phase contact line is still higher in the CAHF droplet compared to H_2O droplet, as demonstrated in Fig. 5 (e). Like temperature distribution observed at time t = 1 s and t = 20 s, a low temperature zone in the CAHF droplet near the droplet vertical axis of symmetry is noticed at time t = 40 s, as shown in Fig. 5 (f). Moreover, in the CAHF droplet, the concentration gradient of suspended hybrid nanoparticles further increases at time t = 40 s compared to time t = 1 s and t = 20 s. At time t = 40 s, a higher concentration of hybrid nanoparticles near the flow vortex compared to droplet interfacial regions and vertical axis of symmetry can be observed, as demonstrated in Fig. 5 (e). This high concentration gradient at time t = 40 s creates a shear viscous flow regime resulting in reduced flow velocity near the vortex region. On the other hand, high flow velocities are observed in relatively low viscosity regions near droplet vertical symmetrical axis and droplet-air interface. Fig. 5 corresponds to 3 μl droplet volume at substrate temperature of T_s = 60 °C for which there exists a negligible difference in evaporation rates between CAHF droplet and H_2O droplet, as demonstrated in Fig. 2 (c). For this reason, the CAHF and H_2O droplets seem identical in Fig. 5. Moreover, Fig. 5 shows droplet evaporation only up to t = 40 s while CAHF and H_2O droplets show some difference in droplet height near the end of evaporation.

As all investigated droplet volumes (3 - 60 µl) show similar velocity and temperature profiles over a plain heated copper substrate, these results are only discussed for a 3 µl droplet volume in Fig. 6. Fig. 6 (a) and (b) show fluid velocity and temperature profiles, respectively, along the droplet height (*h,* as shown in Fig. 1 (a)) for 3 µl volume of CAHF and H_2O droplets on a plain copper surface at T_s = 60 °C. It is noticeable that the peak velocity magnitude in the CAHF droplet exceeds the H_2O droplet peak velocity by 45% and 8% at droplet evaporation time of t = 20 s and t = 40 s, respectively. The high velocity magnitude is due to stronger Marangoni forces in the CAHF droplet compared to H_2O droplet, as shown in Fig. 4. This results in a well-mixed flow thus lowering the mean internal temperature of the CAHF droplet compared to H_2O droplet, as shown in Fig. 6 (b).

Fig. 6 (c, d) illustrates similar velocity and temperature plots for T_s = 80 °C as obtained for T_s = 60 °C in Fig. 6 (a, b), where the CAHF droplet exhibits higher velocity magnitude and lower temperature compared to H_2O droplet. Moreover, the velocity magnitude increases in both CAHF and H_2O droplets due to the higher thermal Marangoni convection at T_s = 80 °C, compared to that observed at T_s = 60 °C. In Fig. 6 (e), the CAHF droplet exhibits higher mean velocity than H_2O droplet at T_s = 100 °C. This results in a lower mean temperature for the CAHF droplet compared to the H_2O droplet at time t = 1 s. However, at time t = 5 s, this behavior is reversed where H_2O droplet shows lower mean droplet temperature than the CAHF droplet, as demonstrated in Fig. 6 (f). This may be due to strong thermal Marangoni convection currents in both H_2O and CAHF droplets at a high substrate temperature of T_s = 100 °C. The results of Fig. 5 and Fig. 6 suggest that enhanced evaporation rate in CAHF droplets is due to higher velocity magnitude and lower mean internal temperature than that of H_2O droplets. Moreover, large thermal Marangoni forces and suspended hybrid nanoparticles facilitate heat transfer between the droplet-substrate and droplet-air interfaces, resulting in reduced mean internal temperature and augmented evaporation rates in CAHF droplets compared to H_2O droplets.

Fig. 7 (a-c) shows the comparison of fluid velocity and hybrid (copper and alumina) nanoparticle velocity profiles for different time instants during evaporation of a 3 µl CAHF droplet at T_s = 60 °C. In Fig. 7, the hybrid nanofluid droplet was treated as a non-homogenous two-phase droplet,

where the velocities of dispersed phase Cu and Al_2O_3 nanoparticles inside the CAHF droplet were separately investigated and compared with the continuum liquid phase that surrounds the dispersed hybrid nanoparticles within the CAHF droplet. As the concentration of suspended hybrid nanoparticles is very low due to high shear stresses along the droplet vertical axis of symmetry (h, as shown in Fig. 1 (a)), the fluid and hybrid nanoparticle velocity profiles are compared at a slight offset from the droplet vertical axis of symmetry h (i.e., at $r = 0.03\ R$). It can be observed that both copper and alumina nanoparticles exhibit a slip velocity, where their velocity magnitude is different from surrounding fluid molecules. The hybrid nanoparticle slip may be due to hydrodynamic forces (such as drag and lift forces) from surrounding fluid molecules. It is also noticeable that copper nanoparticles exhibit lower average velocity with high fluctuations along the droplet height than alumina nanoparticles. This may be due to the large diameter and high density of copper nanoparticles compared to alumina nanoparticles. The slip in hybrid nanoparticle velocity is also observed for different time instants during the CAHF droplet evaporation at T_s = 80 °C, as demonstrated in Fig. 7 (d-f). Due to enhanced thermophoretic forces at elevated temperatures, the hybrid nanoparticles exhibit higher velocity magnitude at T_s = 80 °C compared to that at T_s = 60 °C. Furthermore, the copper nanoparticles show a similar behavior of high fluctuations with lower mean velocity than alumina nanoparticles, as observed for T_s = 60 °C. However, at T_s = 100 °C, both copper and alumina nanoparticles exhibit large fluctuations with similar mean velocity, as illustrated in Fig. 7 (g, h). This may be due to strong internal convection that affects the dynamics of copper and alumina nanoparticles in a similar way at T_s = 100 °C. Although Cu and Al_2O_3 nanoparticles move at different velocities within a heated CAHF droplet owing to their different densities, shape and size, their composition remains the same as initial composition of 50% each. This is because only liquid part evaporates from an evaporating CAHF droplet whjle the dispersed hybrid nanoparticles remain within the droplet and finally form a residue at the end of the CAHF droplet evaporation.

4.2. Boiling performance of CAHF droplets compared to H_2O droplets

Fig. 8 (a) shows the evaporation rate of H_2O and CAHF droplets over a plain copper surface for nucleate, transition and film boiling regimes. It is noticed that the CAHF droplet evaporation rate is up to 10 times that of H_2O droplets in the nucleate boiling region. This is because the droplet boiling is more vigorous and agitated due to the presence of hybrid nanoparticles in CAHF droplets

577 compared to H_2O droplets. In the nucleate boiling region, the droplet evaporation rate
578 tremendously increases at increasing substrate temperature. For considered droplet volumes, the
579 evaporation rate enhancement is up to 62 times for CAHF droplets compared to 16 times for H_2O
580 droplets on a plain copper surface with increasing surface temperature from 103 °C to 125 °C. This
581 suggests a tremendous amount of heat can be removed using CAHF droplets due to their
582 significantly high evaporation rates, making them more suitable for effective cooling of high flux
583 devices compared to water droplets. In droplet boiling experiments, the highest droplet evaporation
584 rate was obtained at the critical point (C_p), as illustrated in Fig. 8 (a). However, two critical points
585 ($C_{p,1}$ and $C_{p,2}$) are observed depending on CAHF and H_2O droplet volumes. The 3 µl and 15 µl
586 volume droplets enter transition boiling regime at relatively lower surface temperatures ($C_{p,1}$) than
587 30 µl and 60 µl volume droplets ($C_{p,2}$). This is because small droplets have reduced effective
588 contact area with the heated surface than large droplets due to the presence of bubbles at the
589 droplet-solid interface. Increasing substrate temperature beyond the critical point further decreases
590 the droplet contact area until a Leidenfrost point (L_p) is reached, where droplet rolls over the vapour
591 cushion on a copper surface (Leidenfrost effect) resulting in low evaporation rates, as illustrated
592 in Fig. 8 (a). The CAHF and H_2O droplets exhibit almost the same evaporation rates in the film-
593 boiling region as they both experience the Leidenfrost effect.
594
595 Fig. 8 (b) shows evaporation rate of a 3 µl CAHF droplet over plain copper and porous residue
596 surfaces for nucleate boiling region. As droplets move over a heated surface in transition boiling
597 and film boiling regions, the residue effect on the following droplet evaporation rate is only studied
598 in the nucleate boiling regime. It is noticeable that the CAHF droplet evaporation rate is enhanced
599 up to 9 times on a porous residue surface compared to a plain copper surface. This is mainly due
600 to higher droplet spreading over a partially wetted residue surface compared to a non-wetted
601 copper surface. However, the effect of droplet residue size (V_{fd}/V_{sd} = 5, 10 and 20) on the
602 subsequent droplet evaporation rate is not very clear due to a non-uniform residue surface obtained
603 in the nucleate boiling region.
604

4.2.1. Mechanistic behaviour of improved boiling performance for CAHF droplets

4.2.1.1. Latent heat flux

Fig. 9 demonstrates the latent heat flux for various volumes of H_2O droplets over a plain copper surface and CAHF droplets over plain copper and porous residue surfaces (V_{fd}/V_{sd} = 20) in the nucleate boiling region. The droplet latent heat flux is only studied in the nucleate boiling region as higher evaporation rates are achieved in this region compared to transition or film boiling regimes. The droplet latent heat flux is obtained as $Q = \rho E h_{fg}/A_c$, where h_{fg} is the latent heat of vaporization ($h_{fg,CAHF}$ =2330.1$\pm$48.3 kJ/kg and $h_{fg,H2O}$ =2259$\pm$25.8 kJ/kg), A_c is the droplet-substrate interfacial area, E is the evaporation rate of the boiling droplet and ρ is the water density (since only water from CAHF droplet evaporates leaving behind a residue of hybrid nanoparticles). It can be observed in Fig. 9 that the latent heat flux increases with increasing substrate temperature for both CAHF and H_2O droplets, exhibiting the maximum heat flux at T_s = 125 °C. Moreover, increasing droplet volume leads to decreasing latent heat flux for both CAHF and H_2O droplets due to the increase in droplet-solid contact area. Despite such similarities between CAHF and H_2O droplets, CAHF droplets exhibit substantially higher latent heat flux than H_2O droplets for similar droplet volumes in the nucleate boiling region, as demonstrated in Fig. 9. It is noticeable that the latent heat flux up to 10 times can be achieved using the CAHF droplet compared to H_2O droplet on a plain heated copper surface. This is due to high latent heat of vaporization along with enhanced evaporation rate resulting in augmented heat flux in CAHF droplets compared to H_2O droplets. This shows enhanced heat removal capability of CAHF droplets at even low particle concentration of 0.1% volume fraction compared to H_2O droplets. These results also suggest that the CAHF can be a better candidate than existing fluids (for instance water) for droplet-based (spray or hotspot) cooling in high heat flux applications. Furthermore, despite higher evaporation rate of the CAHF droplet on its porous residue surface than on a plain copper surface (as illustrated in Fig. 8 (b)), the latent heat flux of a 3 µl CAHF droplet over a residue surface is less than that on a plain copper surface, as shown in Fig. 9. This is because the subsequent CAHF droplet spreads more on its partially wetting residue surface than on a non-wetted copper surface, as shown in Fig. 9 insets. This increases the droplet-solid contact area of the CAHF droplet over the residue surface resulting in reduced latent heat flux.

4.2.1.2. Boiling dynamics

Fig. 10 demonstrates the comparison between boiling dynamics of the CAHF droplet and H_2O droplet over a heated copper surface in the nucleate boiling regime. For a water droplet at T_s = 105 °C, it can be observed that bubble nucleation starts at t = 0.16s. At t = 1.44s, multiple bubbles can be observed suggesting several nucleation sites at the droplet-solid interface inside the water droplet. At t = 2.4s, the bubbles merge into a big bubble that eventually bursts and escapes the water droplet surface. However, the water droplet still maintains its spherical shape despite multiple events of bubble formation and collapse during the droplet boiling process. Conversely, the CAHF droplet experiences shape variations during droplet boiling at T_s = 105 °C. This is due to the suspension of thermally conductive copper-alumina hybrid nanoparticles within the CAHF droplet transferring their high thermal energy to surrounding water molecules that disrupt the CAHF droplet shape. Consequently, the CAHF droplet ejects a few small droplets as observed at t = 2.52s and t = 4.36s, which is not the case with the H_2O droplet at T_s = 105 °C. At T_s = 115 °C, the bubbles are observed inside the water droplet at t = 0.63s that eventually grow and occupy the water droplet surface, as observed at t = 10.32s. As bubbles reach the water droplet surface, the nucleation sites are available at droplet-solid interface for new bubbles to form and grow, as demonstrated at t = 10.32s. The bubbles at water droplet surface eventually burst and more bubbles from nucleation sites grow and occupy the water droplet surface, as noticed at t = 14.6s. This process continues until the water droplet completely evaporates. The high density of bubbles inside the water droplet offers thermal resistance that slows down the droplet boiling process. Unlike water droplet at T_s = 115 °C, the CAHF droplet exhibits early shape variations and eject multiple small droplets due to the agitation induced by suspended copper-alumina hybrid nanoparticles, as observed at t = 0.33s and t = 1.18s. The increasing hybrid nanoparticle concentration with progressive evaporation of the CAHF droplet induces further agitation that erupts numerous tiny droplets resulting in rapid droplet evaporation, as demonstrated at t = 2s and t = 2.06s. At T_s = 125 °C, the highly agitated H_2O and CAHF droplets release multiple small droplets resulting in high droplet evaporation rate. However, early initiation of multiple droplet ejection process due to suspended hybrid nanoparticles evaporates the CAHF droplet long before the water droplet. Moreover, part of the CAHF droplet instantaneously lifts-off the heated copper surface releasing energy from thermally conductive hybrid nanoparticles, as observed at t = 0.06s. Upon subsequent re-contact of droplet lift-off part with the heated copper surface, several tiny droplets are released,

as demonstrated at $t = 0.1$s. The instantaneous lift-off and re-contact process continue until the end of the CAHF droplet boiling. Conversely, at T_s = 125 °C, the water droplet does not exhibit the lift-off mechanism, suggesting relatively low agitation that delays its evaporation time compared to the CAHF droplet.

5. Conclusions

In this research, the phase change dynamics of the CAHF droplet over heated plain copper and porous residue (formed by the evaporation of the first CAHF droplet on a plain copper surface) surfaces was investigated. It was demonstrated that the evaporation rate for CAHF droplets resting on their partially wetting residue surfaces substantially improved compared to that on a non-wetted plain copper surface in sub-boiling and nucleate boiling regimes. As a benchmark in this study, water droplets were used to compare enhanced evaporation and boiling performance of CAHF droplets. This study also revealed that improved thermal Marangoni convection effects, besides enhanced thermal conductivity, resulted in higher evaporation rates in CAHF droplets compared to water droplets. Moreover, increased agitation due to suspended hybrid nanoparticles in CAHF droplets resulted in their improved boiling performance as compared to water droplets on a heated plain copper surface. Based on the results, following are the key outcomes of this research:

- The evaporation rate of CAHF droplets is enhanced up to 24% that of water droplets over a plain copper substrate for T_s = 25-100 °C.
- In the nucleate boiling region, the CAHF droplet evaporation rate is enhanced up to 13 times that of water droplets.
- The latent heat flux up to 10 times can be achieved using the CAHF droplets compared to H_2O droplets on a plain copper surface in the nucleate boiling regime.
- The evaporation rate of the following CAHF droplet on a residue surface rises up to 141% and 800% that on a plain copper surface in sub-boiling and nucleate boiling regimes, respectively.
- The high thermal Marangoni convection in CAHF droplets results in higher internal velocity and lower internal mean temperature than H_2O droplets.

Acknowledgements

The funding for this research is provided by the Hong Kong PhD Fellowship Scheme (HKPFS), the Hong Kong Research Grant Council via Collaborative Research Fund (CRF) account C6022-16G, General Research Fund (GRF) accounts 16206918 & 17205419 and Early Career Scheme (ECS) account 21200819.

References

[1] C.Y. Tso, C.Y.H. Chao, Study of enthalpy of evaporation, saturated vapor pressure and evaporation rate of aqueous nanofluids, Int. J. Heat Mass Transf. 84 (2015) 931–941. https://doi.org/10.1016/j.ijheatmasstransfer.2015.01.090.

[2] S. Fu, C. Tso, Y. Fong, C.Y.H. Chao, Evaporation of Al2O3-water nanofluids in an externally micro-grooved evaporator, Sci. Technol. Built Environ. 23 (2017) 345–354. https://doi.org/10.1080/23744731.2016.1250562.

[3] C.Y. Tso, S.C. Fu, C.Y.H. Chao, A semi-analytical model for the thermal conductivity of nanofluids and determination of the nanolayer thickness, Int. J. Heat Mass Transf. 70 (2014) 202–214. https://doi.org/https://doi.org/10.1016/j.ijheatmasstransfer.2013.10.077.

[4] S. Kakac, A. Pramuanjaroenkij, Analysis Of Convective Heat Transfer Enhancement By Nannofluids: Single-Phase And Two-Phase Treatments, J. Eng. Phys. Thermophys. 89 (2016) 758–793. https://doi.org/10.1007/s10891-016-1437-1.

[5] D. Yoo, Thermal Conductivity of Al2O3/Water Nanofluids, J. Korean Phys. Soc. 51 (2007) 84–87.

[6] S. Akilu, K. V. Sharma, A.T. Baheta, R. Mamat, A review of thermophysical properties of water based composite nanofluids, Renew. Sustain. Energy Rev. 66 (2016) 654–678. https://doi.org/10.1016/j.rser.2016.08.036.

[7] F.R. Siddiqui, C.Y. Tso, K.C. Chan, S.C. Fu, C.Y.H. Chao, Dataset on critical parameters of dispersion stability of Cu/Al2O3 nanofluid and hybrid nanofluid for various ultra-sonication times, Data Br. 22 (2019) 863–865.

[8] L. Yang, J. Xu, K. Du, X. Zhang, Recent developments on viscosity and thermal

conductivity of nanofluids, Powder Technol. 317 (2017) 348–369. https://doi.org/10.1016/j.powtec.2017.04.061.

[9] F.R. Siddiqui, C.Y. Tso, K.C. Chan, S.C. Fu, C.Y.H. Chao, On trade-off for dispersion stability and thermal transport of Cu-Al2O3 hybrid nanofluid for various mixing ratios, Int. J. Heat Mass Transf. 132 (2019) 1200–1216. https://doi.org/https://doi.org/10.1016/j.ijheatmasstransfer.2018.12.094.

[10] M.J. Nine, H. Chung, M.R. Tanshen, N.A.B.A. Osman, H. Jeong, Is metal nanofluid reliable as heat carrier?, J. Hazard. Mater. 273 (2014) 183–191. https://doi.org/10.1016/j.jhazmat.2014.03.055.

[11] J.A.R. Babu, K.K. Kumar, S.S. Rao, State-of-art review on hybrid nanofluids, Renew. Sustain. Energy Rev. 77 (2017) 551–565. https://doi.org/10.1016/j.rser.2017.04.040.

[12] J. Sarkar, P. Ghosh, A. Adil, A review on hybrid nanofluids: Recent research, development and applications, Renew. Sustain. Energy Rev. 43 (2015) 164–177. https://doi.org/https://doi.org/10.1016/j.rser.2014.11.023.

[13] N.A. Che Sidik, M. Mahmud Jamil, W.M.A. Aziz Japar, I. Muhammad Adamu, A review on preparation methods, stability and applications of hybrid nanofluids, Renew. Sustain. Energy Rev. (2017). https://doi.org/10.1016/j.rser.2017.05.221.

[14] M.U. Sajid, H.M. Ali, Thermal conductivity of hybrid nanofluids : A critical review, Int. J. Heat Mass Transf. 126 (2018) 211–234. https://doi.org/10.1016/j.ijheatmasstransfer.2018.05.021.

[15] M. Batmunkh, M.R. Tanshen, M.J. Nine, M. Myekhlai, H. Choi, H. Chung, Thermal Conductivity of TiO2 Nanoparticles Based Aqueous Nanofluids with an Addition of a Modified Silver Particle, Ind. Eng. Chem. Res. 53 (2014) 8445–8451. https://doi.org/10.1021/ie403712f.

[16] M.J. Nine, M. Batmunkh, J.H. Kim, H.S. Chung, H.M. Jeong, Investigation of Al2O3-MWCNTs Hybrid Dispersion in Water and Their Thermal Characterization, J. Nanosci. Nanotechnol. 12 (2012) 4553–4559. https://doi.org/10.1166/jnn.2012.6193.

[17] S. Suresh, K.P. Venkitaraj, P. Selvakumar, M. Chandrasekar, Synthesis of Al2O3–Cu/water

751 hybrid nanofluids using two step method and its thermo physical properties, Colloids
752 Surfaces A Physicochem. Eng. Asp. 388 (2011) 41–48.
753 https://doi.org/https://doi.org/10.1016/j.colsurfa.2011.08.005.

754 [18] T.A.H. Nguyen, A. V Nguyen, Increased Evaporation Kinetics of Sessile Droplets by Using
755 Nanoparticles, Langmuir. 28 (2012) 16725–16728. https://doi.org/10.1021/la303293w.

756 [19] F.C. Wang, H.A. Wu, Pinning and depinning mechanism of the contact line during
757 evaporation of nano-droplets sessile on textured surfaces, Soft Matter. 9 (2013) 5703–5709.
758 https://doi.org/10.1039/C3SM50530H.

759 [20] R.H. Chen, T.X. Phuoc, D. Martello, Effects of nanoparticles on nanofluid droplet
760 evaporation, Int. J. Heat Mass Transf. 53 (2010) 3677–3682.
761 https://doi.org/https://doi.org/10.1016/j.ijheatmasstransfer.2010.04.006.

762 [21] F.R. Siddiqui, C.Y. Tso, S.C. Fu, C.Y.H. Chao, H.H. Qiu, Experimental Investigation On
763 Silver-Graphene Hybrid Nanofluid Droplet Evaporation And Wetting Characteristics Of Its
764 Nanostructured Droplet Residue, in: Proc. ASME-JSME-KSME 8th Jt. Fluids Eng. Conf.,
765 San Francisco, California, USA. July 28–August 1, 2019. Paper No: AJKFluids2019-5049,
766 V004T06A010, 2019. https://doi.org/https://doi.org/10.1115/AJKFluids2019-5049.

767 [22] F.R. Siddiqui, C.Y. Tso, S.C. Fu, H.H. Qiu, C.Y.H. Chao, Evaporation and wetting behavior
768 of silver-graphene hybrid nanofluid droplet on its porous residue surface for various mixing
769 ratios, Int. J. Heat Mass Transf. 153 (2020) 119618.
770 https://doi.org/https://doi.org/10.1016/j.ijheatmasstransfer.2020.119618.

771 [23] H. Hu, R.G. Larson, Evaporation of a Sessile Droplet on a Substrate, J. Phys. Chem. B. 106
772 (2002) 1334–1344. https://doi.org/10.1021/jp0118322.

773 [24] K. Sefiane, R. Bennacer, Nanofluids droplets evaporation kinetics and wetting dynamics on
774 rough heated substrates, Adv. Colloid Interface Sci. 147–148 (2009) 263–271.
775 https://doi.org/https://doi.org/10.1016/j.cis.2008.09.011.

776 [25] Y.C. Kim, Evaporation of nanofluid droplet on heated surface, Adv. Mech. Eng. 7 (2015)
777 1–8. https://doi.org/10.1177/1687814015578358.

778 [26] A. Al-Sharafi, A.Z. Sahin, B.S. Yilbas, S.Z. Shuja, Marangoni convection flow and heat

779 transfer characteristics of water–CNT nanofluid droplets, Numer. Heat Transf. Part A Appl.
780 69 (2016) 763–780. https://doi.org/10.1080/10407782.2015.1090809.

781 [27] A. Al-Sharafi, H. Ali, B.S. Yilbas, A.Z. Sahin, M. Khaled, N. Al-Aqeeli, F. Al-Sulaiman,
782 Influence of thermalcapillary and buoyant forces on flow characteristics in a droplet on
783 hydrophobic surface, Int. J. Therm. Sci. 102 (2016) 239–253.
784 https://doi.org/https://doi.org/10.1016/j.ijthermalsci.2015.11.013.

785 [28] T. Okawa, K. Nagano, T. Hirano, Boiling heat transfer during single nanofluid drop impacts
786 onto a hot wall, Exp. Therm. Fluid Sci. 36 (2012) 78–85.
787 https://doi.org/https://doi.org/10.1016/j.expthermflusci.2011.08.007.

788 [29] G. Duursma, K. Sefiane, A. Kennedy, Experimental Studies of Nanofluid Droplets in Spray
789 Cooling, Heat Transf. Eng. 30 (2009) 1108–1120.
790 https://doi.org/10.1080/01457630902922467.

791 [30] G. Paul, P.K. Das, I. Manna, Nanoparticle deposition from nanofluid droplets during
792 Leidenfrost phenomenon and consequent rise in transition temperature, Int. J. Heat Mass
793 Transf. 148 (2020) 119110.
794 https://doi.org/https://doi.org/10.1016/j.ijheatmasstransfer.2019.119110.

795 [31] F.R. Siddiqui, C.Y. Tso, S.C. Fu, H.H. Qiu, C.Y.H. Chao, Droplet evaporation and boiling
796 for different mixing ratios of the silver-graphene hybrid nanofluid over heated surfaces, Int.
797 J. Heat Mass Transf. 180 (2021) 121786.
798 https://doi.org/https://doi.org/10.1016/j.ijheatmasstransfer.2021.121786.

799 [32] P.J. Yunker, T. Still, M.A. Lohr, A.G. Yodh, Suppression of the coffee-ring effect by shape-
800 dependent capillary interactions, Nature. 476 (2011) 308–311.
801 https://doi.org/10.1038/nature10344.

802 [33] T.P. Bigioni, X.M. Lin, T.T. Nguyen, E.I. Corwin, T.A. Witten, H.M. Jaeger, Kinetically
803 driven self assembly of highly ordered nanoparticle monolayers, Nat. Mater. 5 (2006) 265–
804 270. https://doi.org/10.1038/nmat1611.

805 [34] H.H. Lee, S.C. Fu, C.Y. Tso, C.Y.H. Chao, Study of residue patterns of aqueous nanofluid
806 droplets with different particle sizes and concentrations on different substrates, Int. J. Heat

807 Mass Transf. 105 (2017) 230–236.
808 https://doi.org/https://doi.org/10.1016/j.ijheatmasstransfer.2016.09.093.

809 [35] M. Amjad, Y. Yang, G. Raza, H. Gao, J. Zhang, L. Zhou, X. Du, D. Wen, Deposition pattern
810 and tracer particle motion of evaporating multi-component sessile droplets, J. Colloid
811 Interface Sci. 506 (2017) 83–92. https://doi.org/https://doi.org/10.1016/j.jcis.2017.07.025.

812 [36] F.R. Siddiqui, C.Y. Tso, S.C. Fu, H. Qiu, C.Y.H. Chao, Droplet Evaporation of Cu– Al2O3
813 Hybrid Nanofluid Over Its Residue and Copper Surfaces: Toward Developing a New
814 Analytical Model, J. Heat Transfer. 143 (2021) 1–11. https://doi.org/10.1115/1.4048970.

815 [37] C.J. Ho, J.B. Huang, P.S. Tsai, Y.M. Yang, Preparation and properties of hybrid water-
816 based suspension of Al2O3 nanoparticles and MEPCM particles as functional forced
817 convection fluid, Int. Commun. Heat Mass Transf. 37 (2010) 490–494.
818 https://doi.org/https://doi.org/10.1016/j.icheatmasstransfer.2009.12.007.

819 [38] Y. Xuan, Z. Yao, Lattice boltzmann model for nanofluids, Heat Mass Transf. 41 (2005)
820 199–205. https://doi.org/10.1007/s00231-004-0539-z.

821 [39] X. Zheng, Z. Silber-Li, The influence of Saffman lift force on nanoparticle concentration
822 distribution near a wall, Appl. Phys. Lett. 95 (2009). https://doi.org/10.1063/1.3237159.

823 [40] M. Bahiraei, Particle migration in nanofluids: A critical review, Int. J. Therm. Sci. 109
824 (2016) 90–113. https://doi.org/10.1016/j.ijthermalsci.2016.05.033.

825 [41] M. Bahiraei, S.M. Hosseinalipour, Particle migration in nanofluids considering
826 thermophoresis and its effect on convective heat transfer, Thermochim. Acta. 574 (2013)
827 47–54. https://doi.org/10.1016/j.tca.2013.09.010.

828 [42] L. Karlsson, A. Ljung, T.S. Lundstrom, Comparing Internal Flow in Freezing and
829 Evaporating Water Droplets Using PIV, Water. 12 (2020) 1489.
830 https://doi.org/10.3390/w12051489.

831 [43] J. Xu, X. Yan, G. Liu, J. Xie, The critical nanofluid concentration as the crossover between
832 changed and unchanged solar-driven droplet evaporation rates, Nano Energy. 57 (2019)
833 791–803. https://doi.org/10.1016/j.nanoen.2019.01.013.

[44] X. Yan, J. Xu, Z. Meng, J. Xie, G. Liu, Multiscale Characteristic in Symmetric/Asymmetric Solar-Driven Nanofluid Droplet Evaporation, Langmuir. 36 (2020) 1680–1690. https://doi.org/10.1021/acs.langmuir.9b03122.

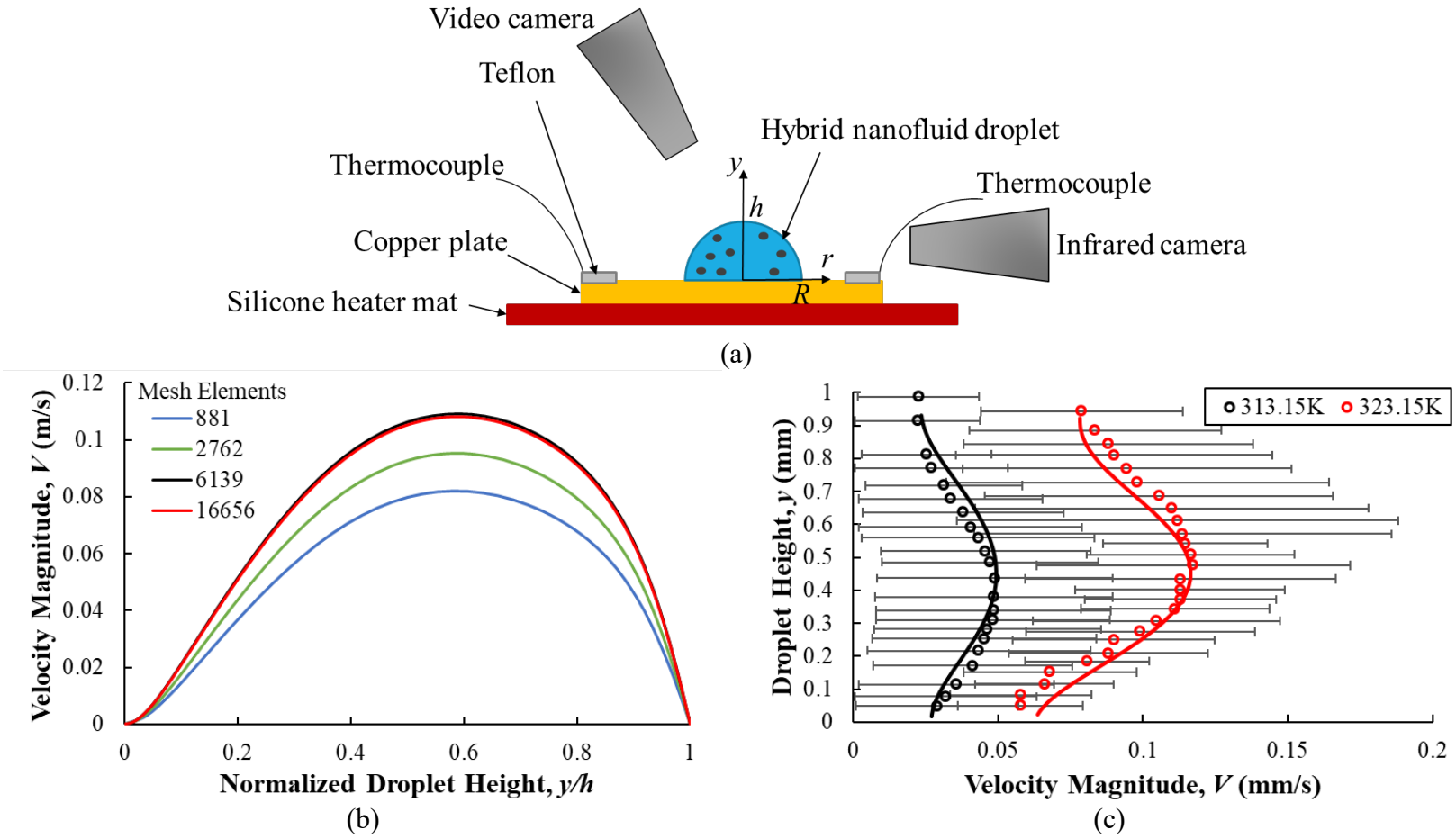

Fig. 1 (a) A schematic of the experimental setup, (b) mesh independence test for the CAHF droplet simulation and (c) numerical model validation using experimental velocity data at $r = 0$ [42]

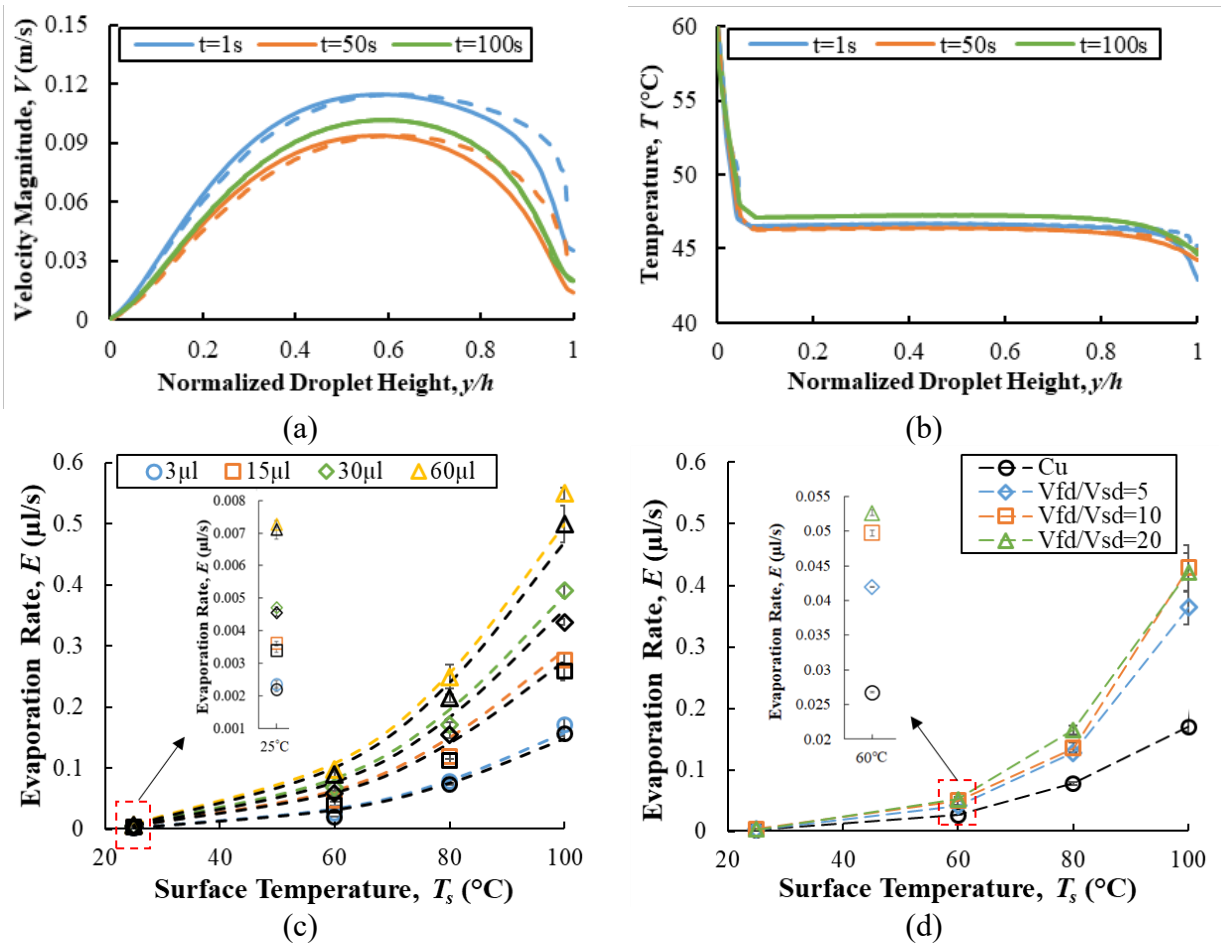

Fig. 2 (a) Comparison of velocity magnitude of a 15 µl CAHF droplet at T_s = 60 °C for no slip (solid lines) and slip (dashed lines) boundary conditions, (b) comparison of temperature profile of a 15 µl CAHF droplet at T_s = 60 °C for no slip (solid lines) and slip (dashed lines) boundary conditions, (c) evaporation rate of H_2O droplets (black markers) and CAHF droplets (colored markers) on a copper surface for different droplet volumes. Dashed lines (black for H_2O droplets and colored for CAHF droplets) are empirical results from equation (8), (d) evaporation rate of a 3 µl volume of the CAHF droplet over copper (black marker) and residue surfaces (colored markers) for various substrate temperatures.

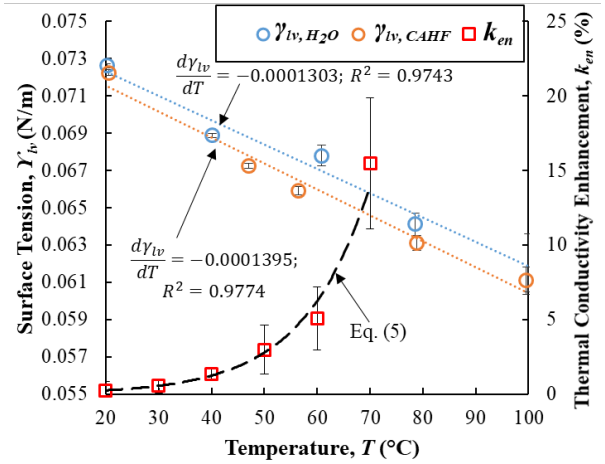

(a)

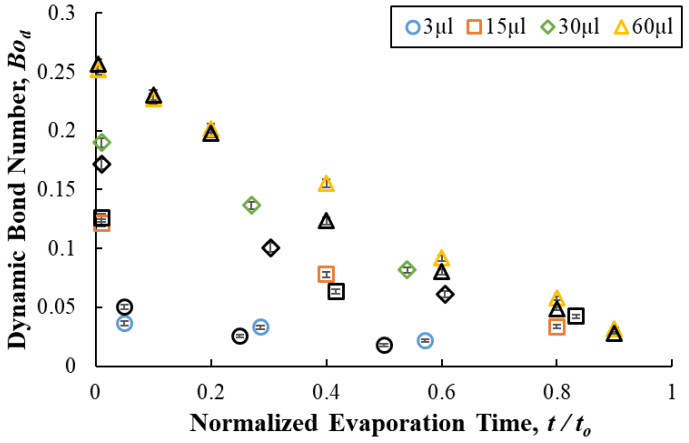

(b)

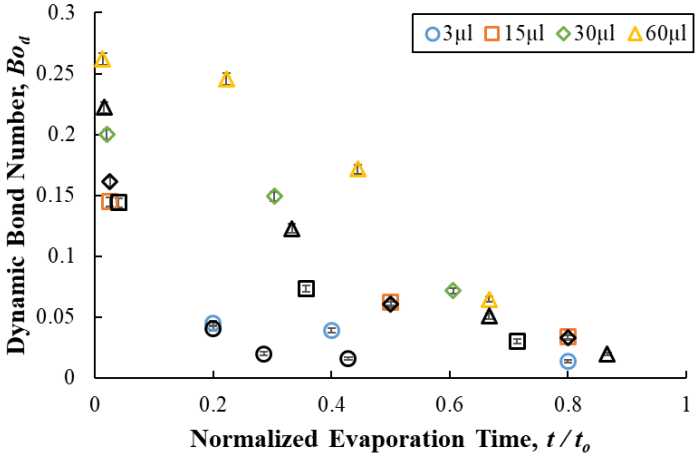

(c)

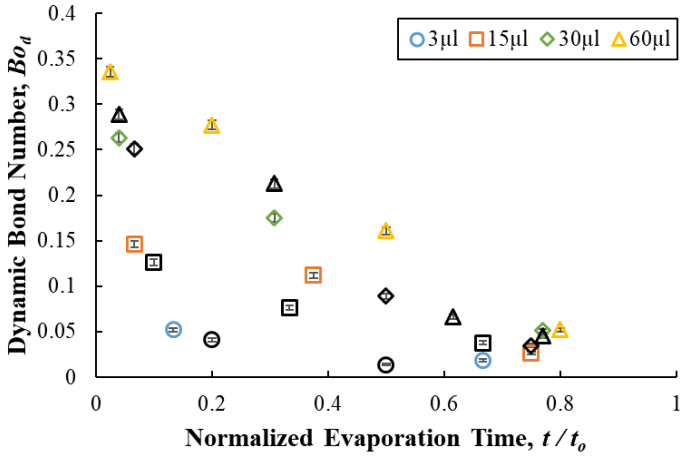

(d)

Fig. 3 (a) CAHF and H_2O surface tension and thermal conductivity plots, (b-d) variation of the dynamic Bond number with evaporation time of H_2O droplets (black markers) and CAHF droplets (colored markers) at a copper plate surface temperature of (b) 60 °C, (c) 80 °C and (d) 100 °C.

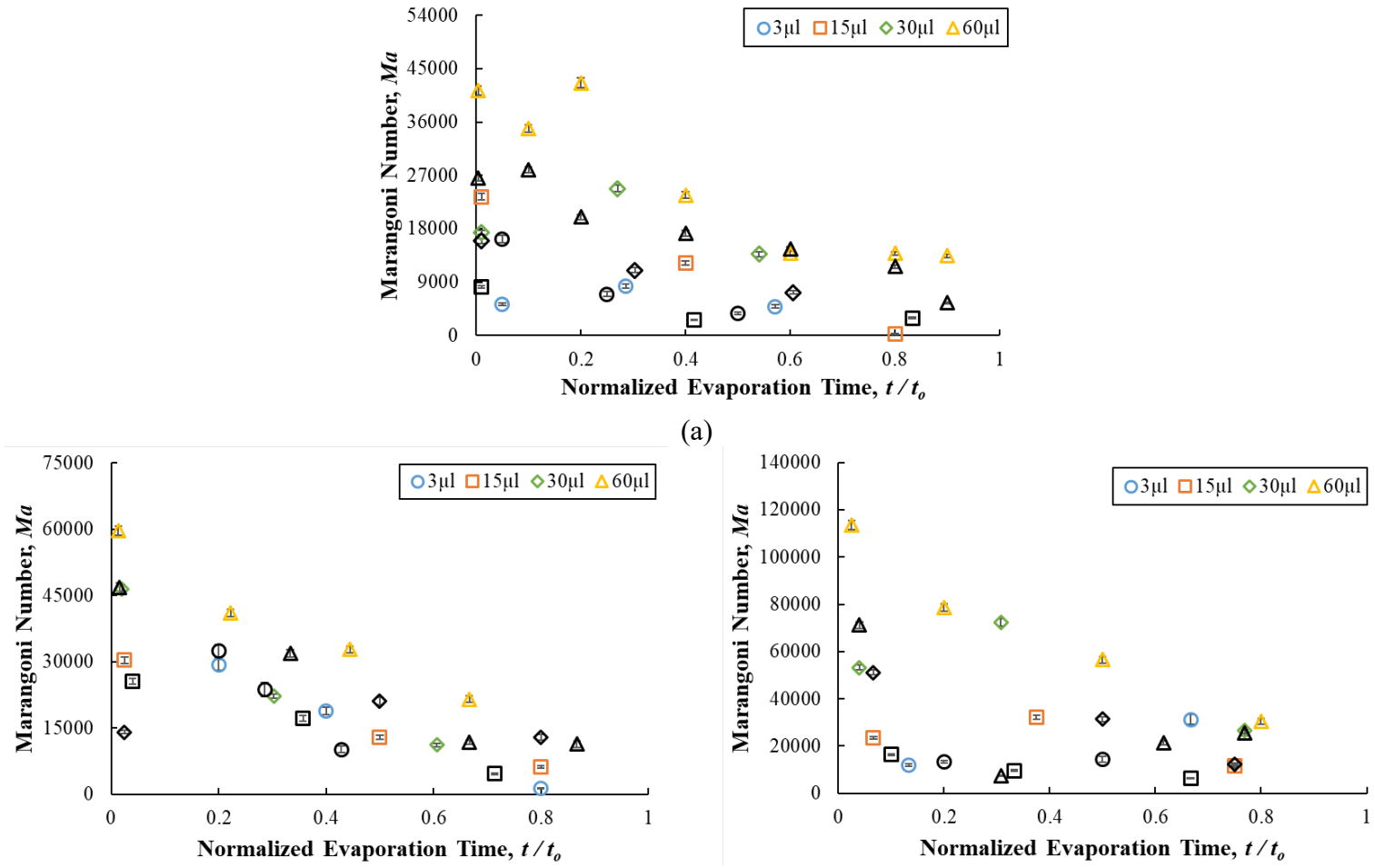

Fig. 4 Variation of the Marangoni number with evaporation time of H_2O droplets (black markers) and CAHF droplets (colored markers) at a copper plate surface temperature of (a) 60 °C, (b) 80 °C and (c) 100 °C.

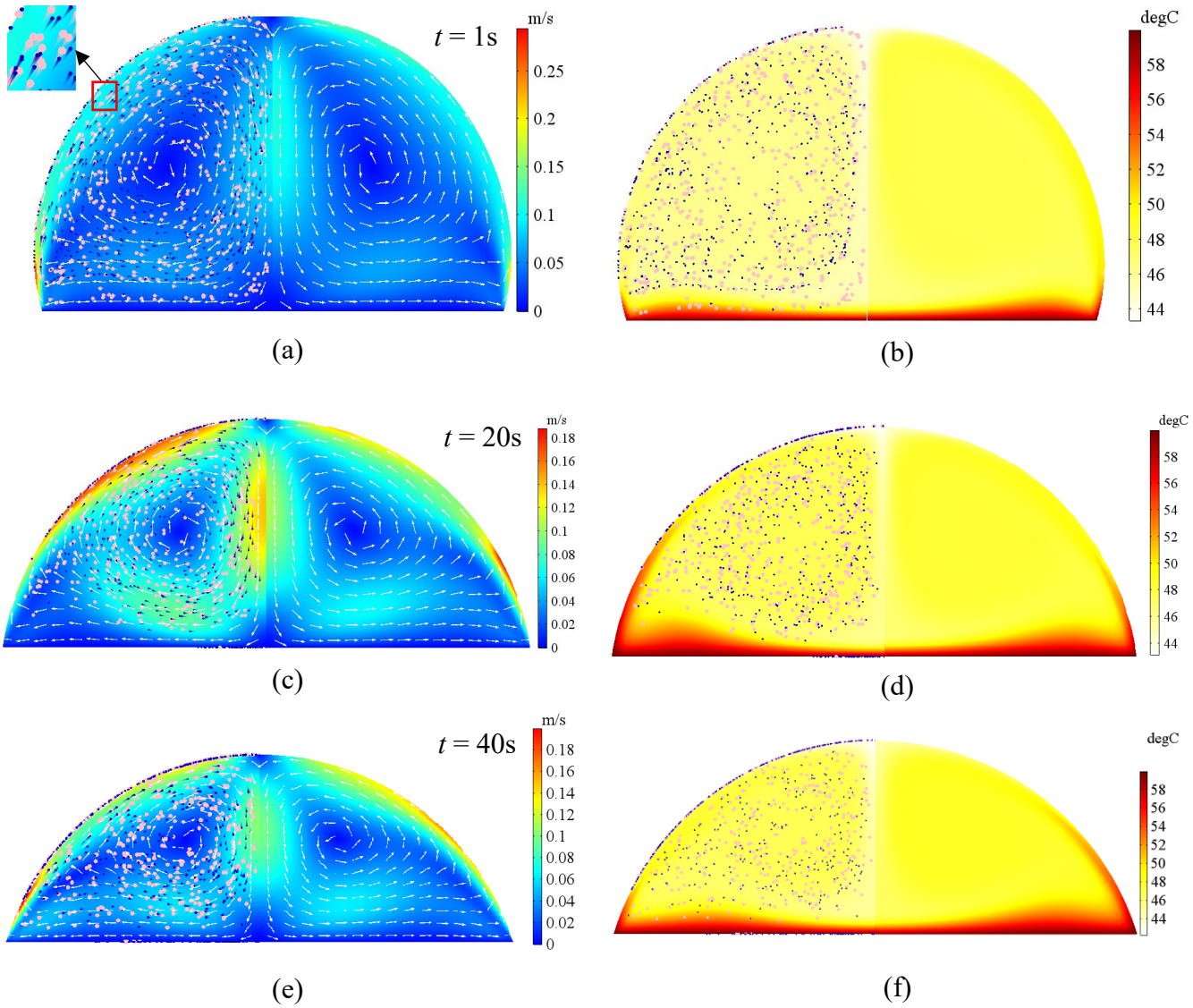

Fig. 5 Comparison of (a, c, e) velocity and (b, d, f) temperature fields of 3 µl CAHF (droplet left half) and H_2O (droplet right half) droplets for different time instants during evaporation at T_s = 60°C. Pink and blue suspended particles are copper and alumina nanoparticles, respectively.

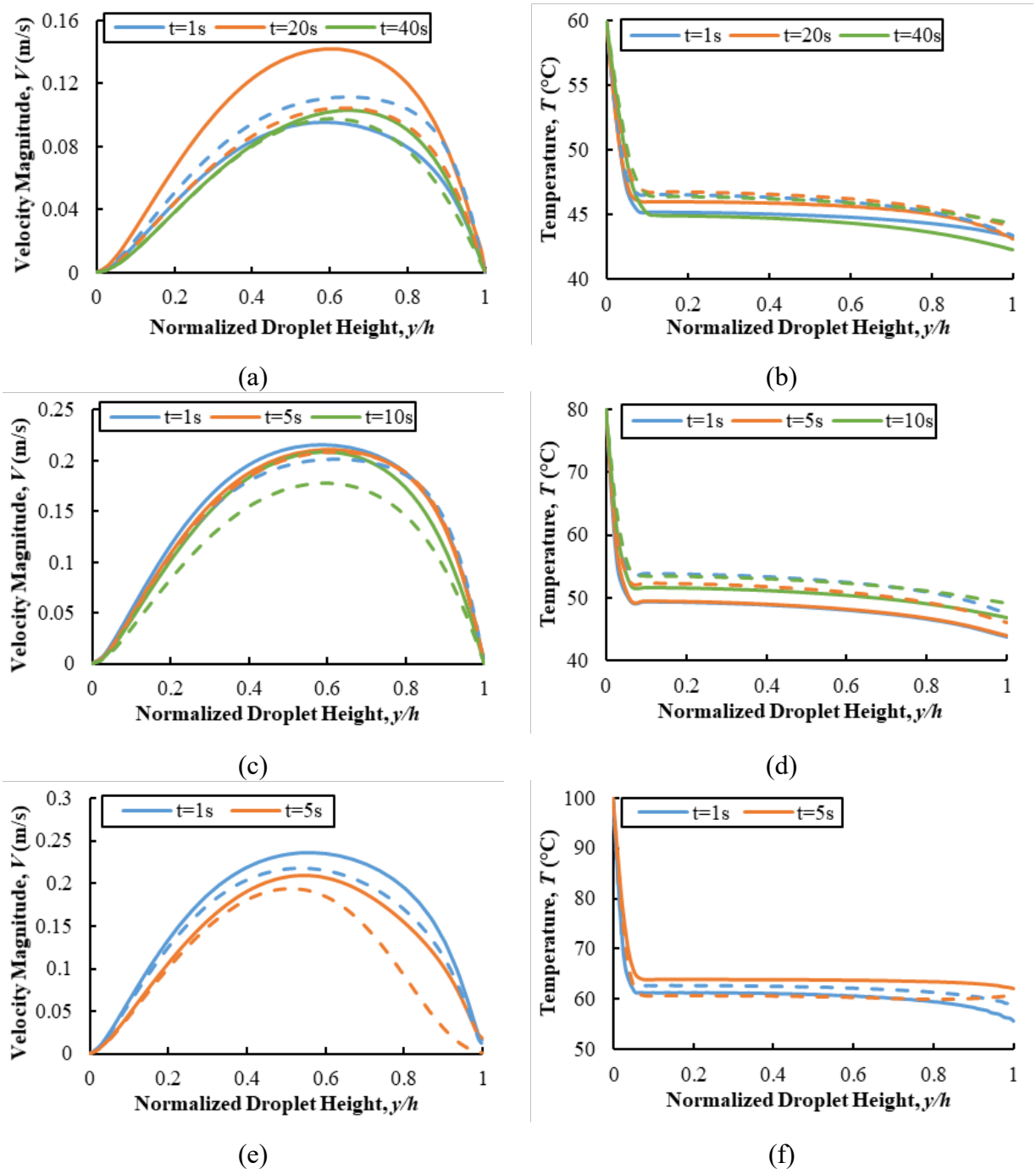

Fig. 6 Variation of fluid (a) velocity and (b) temperature profiles along the droplet height inside a 3 µl droplet at T_s = 60 °C. Solid and dashed lines correspond to CAHF and H_2O droplets, respectively. Plots (c, d) and (e, f) correspond to T_s = 80 °C and T_s = 100 °C, respectively.

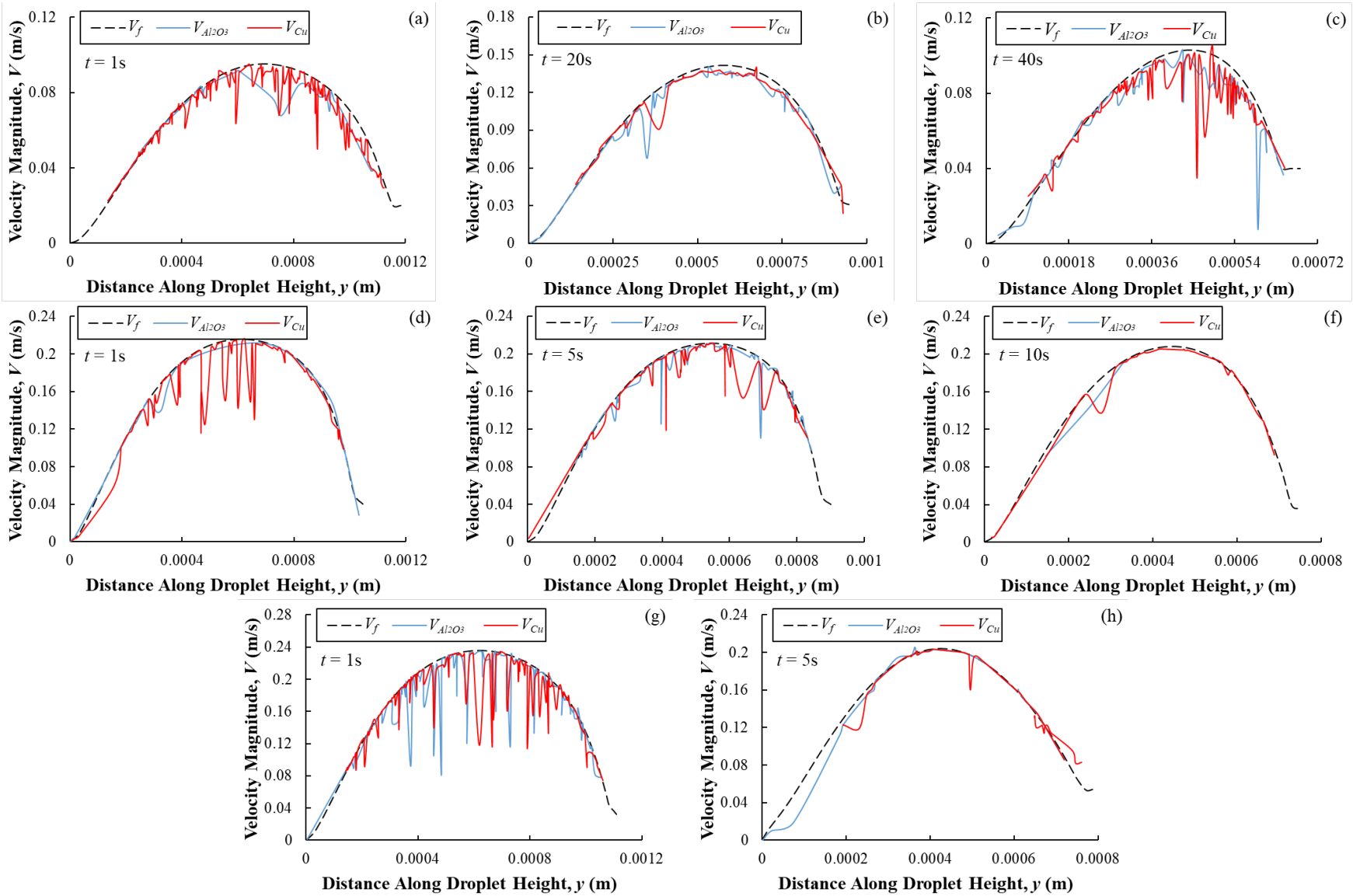

Fig. 7 Comparison of fluid velocity (V_f) and hybrid nanoparticles velocity (V_{Al2O3} and V_{Cu}) along droplet height (at $r = 0.03R$) during evaporation of a 3 µl volume of CAHF droplet at (a-c) T_s = 60 °C, (d-f) T_s = 80 °C and (g, h) T_s = 100 °C.

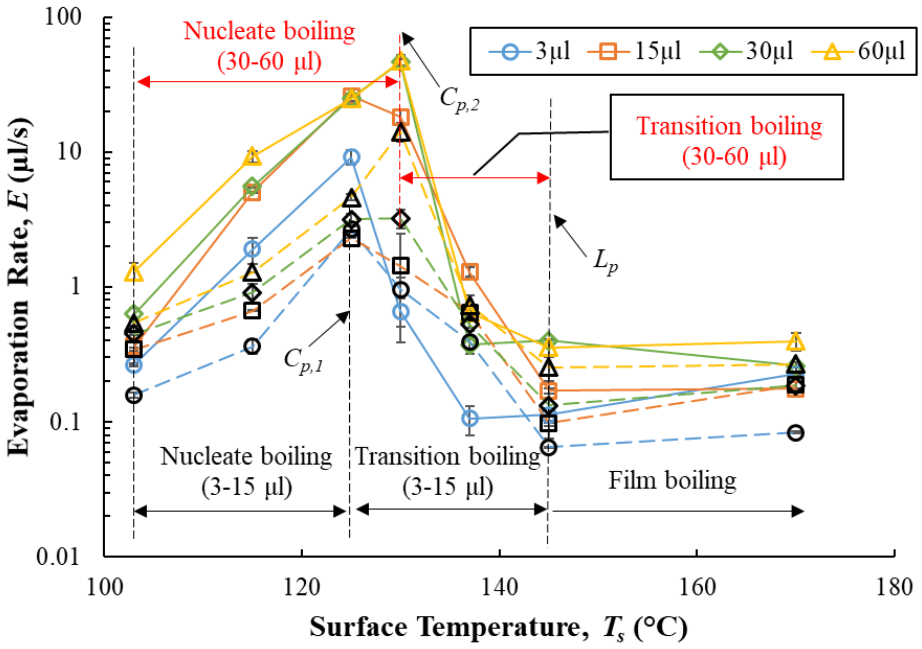

(a)

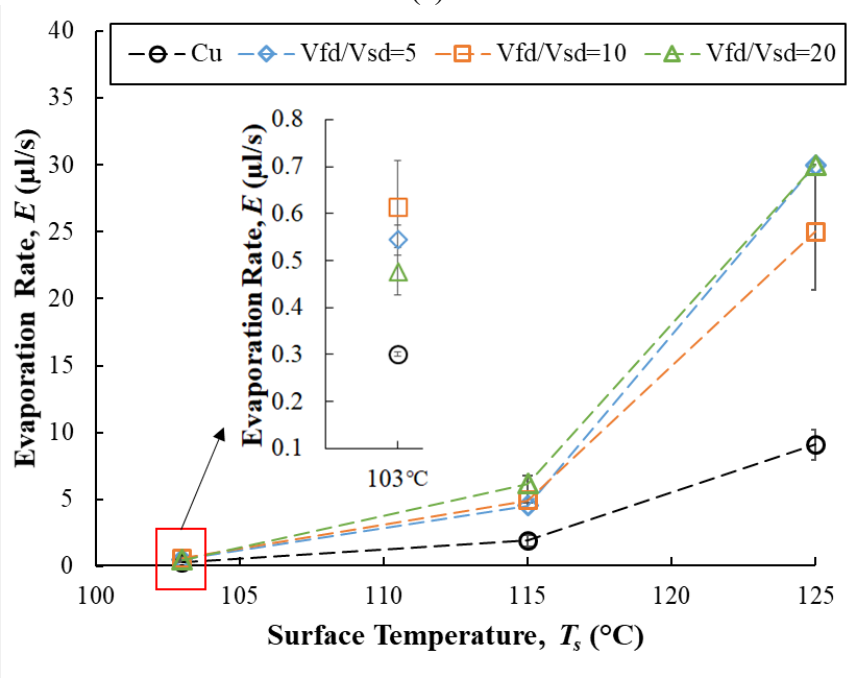

(b)

868 Fig. 8 (a) Evaporation rate of H_2O droplets (black markers, dashed lines) and CAHF droplets
869 (colored markers, solid lines) in different droplet boiling regimes, (b) evaporation rate of a 3 µl
870 CAHF droplet on a copper surface (black markers) and residue surfaces (colored markers) in the
871 nucleate boiling regime.
872

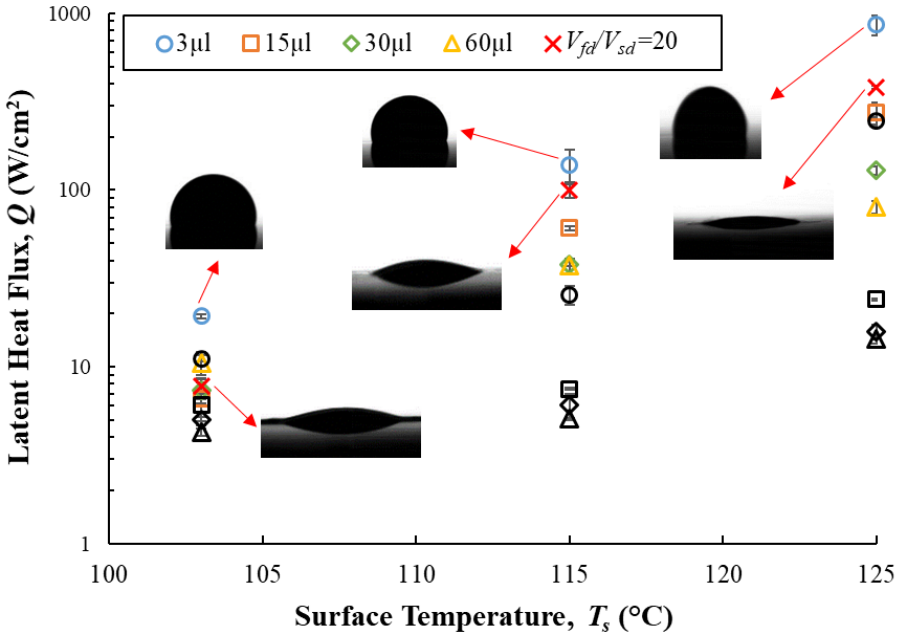

Fig. 9 Latent heat flux of water droplets (black markers) over a copper surface and CAHF droplets (colored markers) over copper and residue surfaces (V_{fd}/V_{sd} = 20) in the nucleate boiling regime. Insets show 3 µl CAHF droplet over copper and residue surfaces.

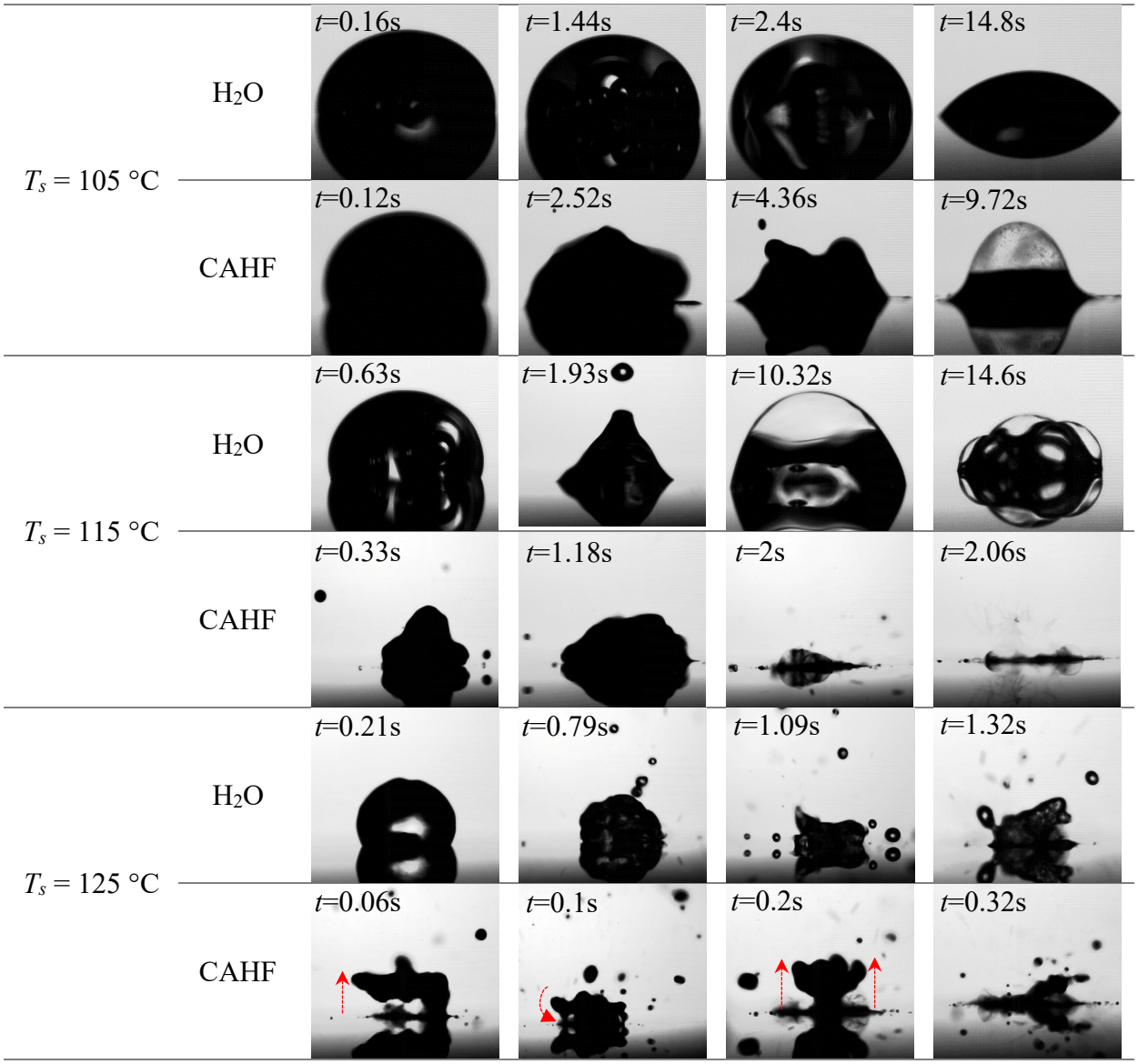

Fig. 10 Comparison in boiling dynamics of 15 µl volume of water and CAHF droplets over a heated copper surface in the nucleate boiling regime.